RSC Advances

PAPER

View Article Online
View Journal | View Issue

Check for updates

Cite this: *RSC Adv.*, 2025, **15**, 19361

Up-conversion luminescence and temperature sensing based on $Ba_3Y(BO_3)_3$:Er^{3+},Yb^{3+} phosphors†

Lei Zhang,‡[a] You Zhang,‡[b] Cuilin Jin,[a] Chunhao Wang,[a] Qiongyu Bai,[a] Yibo Zheng *[a] and Xu Li *[b]

Received 21st February 2025
Accepted 21st May 2025

DOI: 10.1039/d5ra01277e

rsc.li/rsc-advances

Noncontact fluorescence temperature detection systems have become a significant research focus. In this study, a new $Ba_3Y(BO_3)_3$ phosphor co-doped with Er^{3+}/Yb^{3+} was successfully synthesized using a high-temperature solid phase method. The introduction of Yb^{3+} as a sensitizer enhanced the luminescence properties of the $Ba_3Y(BO_3)_3$ phosphor. The occupation of Er^{3+} and Yb^{3+} ions in the crystal lattice was analyzed in detail. The up-conversion luminescence and underlying mechanisms were explained by the double logarithmic relationship between the luminescence intensity and pump power. The temperature sensitivity of the phosphors was explored in the range of 333–513 K using fluorescence intensity ratio technology based on the two green peaks (thermal coupling level Er^{3+}). The temperature sensing S_r reached 1.44 × 10^{-4} K^{-1} at 333 K, indicating that $Ba_3Y(BO_3)_3$:Er^{3+},Yb^{3+} phosphors have potential applications as temperature sensors.

Open Access Article. Published on 09 June 2025. Downloaded on 4/8/2026 5:43:30 AM.
This article is licensed under a Creative Commons Attribution 3.0 Unported Licence.

1. Introduction

Highly sensitive temperature detection is crucial for enhancing both production quality and daily life.[1–3] Noncontact temperature sensing using luminescence thermometry offers advantages such as fast response, high sensitivity, and versatility in various environments, including high temperatures, high pressures and biological systems, making it a topic of significant interest.[4–8] Luminescence thermometry measures changes in the luminescence properties of a system with respect to temperature, enabling temperature characterization. These properties include single-emission peak intensity, emission peak position, fluorescence intensity ratio of two emission peaks, fluorescence lifetime, and emission peak half-width.[9–13] Among these techniques, the fluorescence intensity ratio is the most resistant to interference. Therefore, researchers often focus on developing systems based on fluorescence intensity ratios for temperature measurement.[14–16] Inorganic up-conversion luminescent materials, which have low background noise and excitation bands in the infrared range, have garnered widespread attention in temperature sensing and bioimaging.[17–20] Up-conversion temperature-detecting phosphors are usually doped with Er^{3+}/Yb^{3+} ions, utilizing the two thermally coupled energy levels of Er^{3+} as the temperature measurement energy level.[21–24] Although Yb^{3+} has a larger absorption cross-section and wider absorption band for near-infrared energies, Yb^{3+} ions are often used as sensitizers.[25–28]

Borates, which are known for their diverse crystal structures, good physical stability,[29,30] and low synthesis temperatures,[31,32] are expected to become mainstream phosphors.[33,34] Shangke Pan *et al.* synthesized Nd^{3+}-doped $Ba_3Y(BO_3)_3$ phosphors using the lift-off method, achieving a crystalline phase transition temperature of 1148 °C.[35] Zhao *et al.* explored the luminescence mechanism of Ce^{3+}/Nd^{3+} co-doped $Ba_3Y(BO_3)_3$ phosphors and proposed their application as solar spectral converters in Si-based solar cells.[36] Li *et al.* successfully prepared $Ba_3Y(BO_3)_3$ doped with 24 mol% Eu^{3+} and 1 mol% Bi^{3+} phosphors and demonstrated their potential for application in white LEDs.[37]

To the best of our knowledge, Er^{3+}/Yb^{3+}-doped $Ba_3Y(BO_3)_3$ phosphors have not been extensively studied. In this study, we prepared Er^{3+}/Yb^{3+} co-doped $Ba_3Y(BO_3)_3$ phosphors and thoroughly investigated their structure, morphology, luminescence properties, and energy transfer mechanism between Yb^{3+} and Er^{3+} ions. The two-photon green emission of Er^{3+} was confirmed through the double logarithmic relationship between the power and luminescence intensity. Additionally, we examined the upconversion optical temperature-sensing properties of Er^{3+}/Yb^{3+}-*co*-doped $Ba_3Y(BO_3)_3$ phosphors using the FIR technique.

2. Experimental section

2.1 Sample synthesis

$BaCO_3$, Y_2O_3, H_3BO_3, Er_2O_3 (99.99%), Yb_2O_3 (99.99%), deionized water, and anhydrous ethanol were used to prepare the

[a]*Hebei Key Laboratory of Optoelectronic Information and Geo-detection Technology, College of Gems and Materials, Hebei GEO University, Shijiazhuang 050031, China. E-mail: yibo_zheng@hgu.edu.cn*

[b]*Hebei Key Laboratory of Photo-Electricity Information and Materials, College of Physics Science and Technology, Hebei University, Baoding 071002, China. E-mail: lixcn@sina.com*

† Electronic supplementary information (ESI) available. See DOI: https://doi.org/10.1039/d5ra01277e

‡ Lei Zhang and Meitong Guo are co-first authors of this paper.

© 2025 The Author(s). Published by the Royal Society of Chemistry

Open Access Article. Published on 09 June 2025. Downloaded on 4/8/2026 5:43:30 AM. This article is licensed under a Creative Commons Attribution 3.0 Unported Licence.

phosphors. $Ba_3Y_{1-x}(BO_3)_3$:xEr^{3+} and $Ba_3Y_{0.93-y}(BO_3)_3$:0.07Er^{3+}, yYb^{3+} phosphors were synthesized using a high-temperature solid-state method with molar fractions x = 0.02, 0.03, 0.04, 0.05, 0.06, 0.07, 0.08, and 0.09, and y = 0.07, 0.14, 0.21, 0.28, 0.35, 0.42, 0.49, and 0.56, respectively. The corresponding number of precursors was weighed and ground in an agate mortar and pestle for 10 min. The mixture was then placed in an alumina crucible and pre-annealed in a high-temperature muffle furnace at 1250 °C for 6 h. After cooling to room temperature, the samples were ground into a powder for further analysis.

2.2 Sample characterization details

We used a Bruker D8 Advanced Diffractometer to determine the profile of the synthesized materials through X-ray diffraction (XRD) analysis using Cu Kα radiation (1.5406 Å) over a range of 15–80°. The emission spectra of the samples were obtained using a Pro-FL spectrometer (F-7000, Hitachi, Japan) under 980 nm excitation from a semiconductor laser. Temperature-dependent emission spectra were obtained using the same equipment and a TCB1402C temperature controller (China).

3. Results and discussion

3.1 Structure and morphology of samples

Fig. 1(a) and (b) show the XRD patterns of $Ba_3Y(BO_3)_3$:xEr^{3+} (x = 0.02, 0.03, 0.04, 0.05, 0.06, 0.07, 0.08, 0.09) and $Ba_3Y(BO_3)_3$:0.07Er^{3+},yYb^{3+} (y = 0.07, 0.14, 0.21, 0.28, 0.35, 0.42, 0.95, 0.56) samples. The diffraction patterns are consistent with the standard card PDF#51-1849. No significant impurity peaks were observed, indicating that the Er^{3+} and Yb^{3+} did not change the lattice structure because Er^{3+} and Yb^{3+} ions have similar radii to Y^{3+} ions.[38] The synthesized material was in a pure hexagonal crystalline phase with space group $P6_3\,cm$ (185), with cell parameters $a = b = 9.419$ Å, $c = 17.598$ Å, and a cell volume of 1352.2 $Å^3$.[39] As shown in Fig. 1c, every B atom is coordinated with three O atoms to form triangles [BO_3]. For the Ba atom, two different coordinate methods are coordinated with nine and six O atoms to form polyhedral [Ba_1O_9] and [Ba_2O_6]. Although all the Y atoms are coordinated with six O atoms, there exist two different kinds of polyhedra owing to the difference in the distortion of [Y_1O_6] and [Y_2O_6].[40,41]

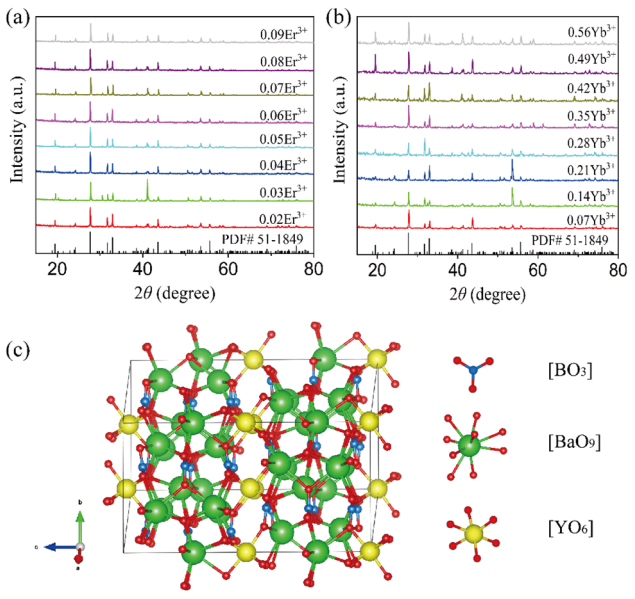

Fig. 1 (a) XRD patterns of $Ba_3Y(BO_3)_3$:xEr^{3+} (x = 0.02, 0.03, 0.04, 0.05, 0.06, 0.07, 0.08, and 0.09) with the standard card of $Ba_3Y(BO_3)_3$. (b) XRD patterns of $Ba_3Y(BO_3)_3$:0.07Er^{3+},yYb^{3+} (y = 0.07, 0.14, 0.21, 0.28, 0.35, 0.42, 0.95, and 0.56) with the standard card of $Ba_3Y(BO_3)_3$. (c) Schematic of the crystal structure of $Ba_3Y(BO_3)_3$.

The SEM patterns of the $Ba_3Y(BO_3)_3$:0.07Er^{3+},0.21Yb^{3+} phosphor are presented in Fig. 2a. It can be observed that the sample exhibits better crystallization, with a size of approximately 3–8 μm. Meanwhile, the element mapping in Fig. 2b–f shows that the main elements Ba, Y, O, Er, and Yb are uniformly distributed in the sample. The EDS measure in Table S1† indicates that the Er and Yb ions are doped in the matrix.

3.2 Optical properties of samples

The diffuse reflection spectrum of 0.07Er^{3+}, 0.21Yb^{3+} phosphor is shown in Fig. S1.† It can be observed that there are some absorption peaks at 297 nm, 379 nm, 488 nm, 521 nm, 651 nm, 970 nm and 1416 nm, respectively. In particular, the strongest band is located at 870–1040 nm, which indicates that it can well absorb light at 980 nm. To investigate the up-conversion luminescence performance of the samples, we tested the emission spectra of samples doped with different concentrations of Er^{3+} ions under 980 nm excitation at room temperature. Fig. 3(a) shows the upconverted emission spectra of $Ba_3Y(BO_3)_3$:xEr^{3+} (x = 0.01, 0.02, 0.03, 0.04, 0.05, 0.06, 0.07, 0.08, 0.09). The spectra reveal the same emission peaks across the samples, consisting of two groups of peaks in the green domain and one group of peaks in the red domain. Generally, different numbers of peaks are in one group of emissions according to the splitting degree of the ground state and excited state in different crystal fields. The peaks at 520 nm, 525 nm and 538 nm are attributed to the transition of $^2H_{11/2} \rightarrow {}^4I_{15/2}$ while the peaks at 549 nm, 553 nm and 563 nm are attributed to the transition of $^4S_{3/2} \rightarrow {}^4I_{15/2}$. The group of red emission peaks at 656 nm, 662 nm, 670 nm, 677 nm, and 684 nm is caused by the $^4F_{9/2} \rightarrow {}^4I_{15/2}$ transition of Er^{3+} ions. All the results confirm the successful incorporation of Er^{3+} ions into the $Ba_3Y(BO_3)_3$ lattice.[42,43] The intensities of the green and red emissions increased consistently with increasing Er^{3+} concentration from 0.01 (x = 0.01). The luminescence intensity reaches a maximum at $x = 0.07$, after which phosphor concentration quenching occurs, leading to a gradual decrease in luminescence intensity with further Er^{3+} doping.

Fig. 3(b) shows the up-conversion emission spectra of phosphor $Ba_3Y(BO_3)_3$:7 mol% Er^{3+},yYb^{3+} (y = 7, 14, 21, 28, 35, 42, 49, and 0.56). When the Yb^{3+} doping concentration was less than 21 mol%, the red emission intensity significantly increased with increasing Yb^{3+} concentration, while the green emission showed no significant relative change; however, the trend in green emission was similar to that of the red emission. At an Yb^{3+} doping concentration of 0.21, the luminous

© 2025 The Author(s). Published by the Royal Society of Chemistry

Open Access Article. Published on 09 June 2025. Downloaded on 4/8/2026 5:43:30 AM.
This article is licensed under a Creative Commons Attribution 3.0 Unported Licence.

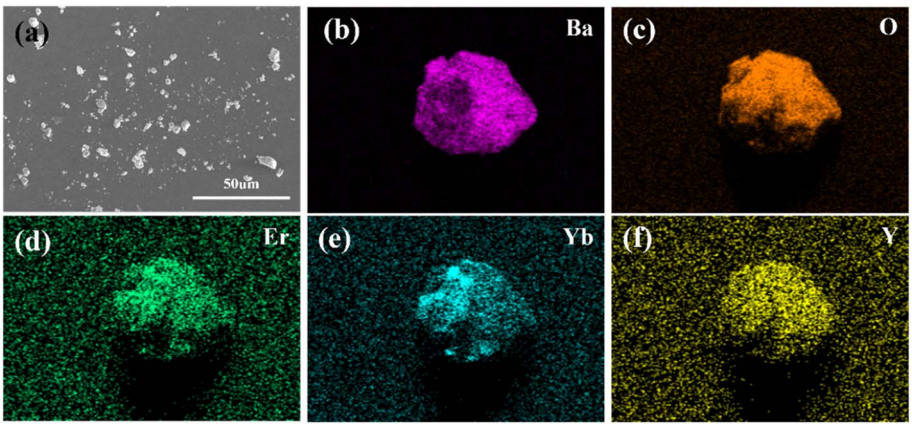

Fig. 2 (a) SEM patterns of $Ba_3Y(BO_3)_3$:0.07Er^{3+},0.21Yb^{3+}. (b)–(f) Elemental mapping of Ba, O, Er, Yb, and Y in $Ba_3Y(BO_3)_3$:0.07Er^{3+},0.21Yb^{3+}.

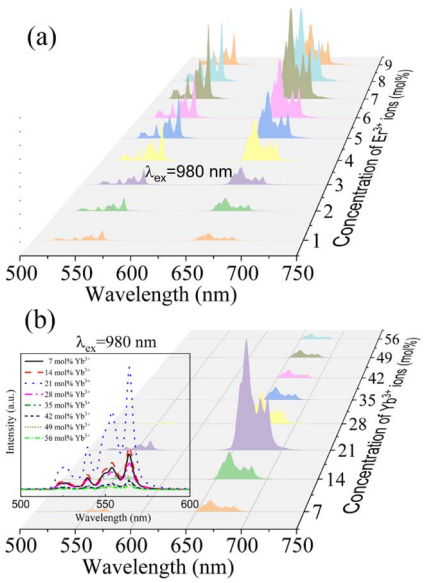

Fig. 3 (a) UCL spectra of (a) $Ba_3Y(BO_3)_3$:xEr^{3+} samples and (b) $Ba_3Y(BO_3)_3$:7mol% Er^{3+},yYb^{3+} samples under 980 nm laser excitation.

intensities of both the green and red emission bands reached their maximum values. Beyond this concentration, further Yb^{3+} doping resulted in decreased luminescence intensity, indicating the onset of concentration quenching at $y = 0.21$. Additionally, with increased Yb^{3+} doping, the EBT process from Er^{3+} to Yb^{3+} was enhanced, as described by the following equation: [$Er^{3+}(^4S_{3/2}) + Yb^{3+}(^2F_{7/2}) \rightarrow Er^{3+}(^4I_{13/2}) + Yb^{3+}(^2F_{5/2})$]. On the one hand, the defect produced in the synthesis process provides an absorption site that promotes the doping of Yb^{3+} ions. On the other hand, energy transfer occurs between the Yb^{3+} ions and non-bridging oxygen defects, which limits the amount of Yb^{3+} doping. However, the doping content of Yb^{3+} and the defect concentration have a nonlinear relationship.[44]

Generally, the luminescence center grows in number, and the distance between the dopant ions decreases with an increase in activator doping concentration, which increases the competition between the radiative transition and the nonradiative (NR) process and influences PL performance. The critical distance (R_c) is an important parameter for expressing the average distance between dopants when the concentration quenching effect occurs and can be expressed as follows:[45]

$$R_c = 2\left(\frac{3V}{4\pi\chi_c N}\right)^{1/3}, \quad (1)$$

where V is the volume (Å^3), χ_c is the quenching concentration, and N is the cation number. In this case, the values of V, χ_c and N are 1352.2 Å^3, 0.07 and 6, respectively. Substituting these values into eqn (1), the value of R_c can be calculated as 18.32 Å, which is greater than 5 Å, and the energy transfer between the dopants is the result of the electric multipolar effect.

To further explain the concentration quenching mechanism of the dopant in the sample, the following equation is used:[46]

$$\log\left(\frac{I}{x}\right) = A - \left(\frac{\theta}{3}\right)\log x, \quad (2)$$

where I represents the emission intensity under the same excitation conditions, x is the concentration of doped ions, and A is the constant related to θ. The concentration quenching mechanism is attributed to the electric dipole–dipole (d–d), dipole–quadrupole (d–q) and quadrupole–quadrupole (q–q) interactions, corresponding to 6, 8 and 10, respectively. As illustrated in Fig. S2 and S3,† the logarithmic coordinate system is built using log(x) and log(I/x) as horizontal and vertical coordinates. According to the linear fitting of experimental data, the linear fitting slopes ($-\theta/3$) are calculated to be −3.96, −4.10, −4.04, −4.01, −3.89, −3.73, −3.72, −4.34 and −3.83, which means that all the values of θ are close to 10, demonstrating that the concentration quenching mechanism of dopant in $Ba_3Y(BO_3)_3$:Er^{3+} and $Ba_3Y(BO_3)_3$:Er^{3+},Yb^{3+} phosphor are attributed to electric q–q interaction.

To further investigate the luminescence mechanism of the Er^{3+}/Yb^{3+} co-doped $Ba_3Y(BO_3)_3$ phosphor, we examined the up-conversion emission spectra of $Ba_3Y(BO_3)_3$:0.07Er^{3+},0.21Yb^{3+} samples under different excitation powers. As shown in Fig. 4a, as the excitation power of the 980 nm laser increased, the up-conversion emission intensity of the samples also increased gradually. When the up-conversion emission is in a non-

Open Access Article. Published on 09 June 2025. Downloaded on 4/8/2026 5:43:30 AM.
This article is licensed under a Creative Commons Attribution 3.0 Unported Licence.

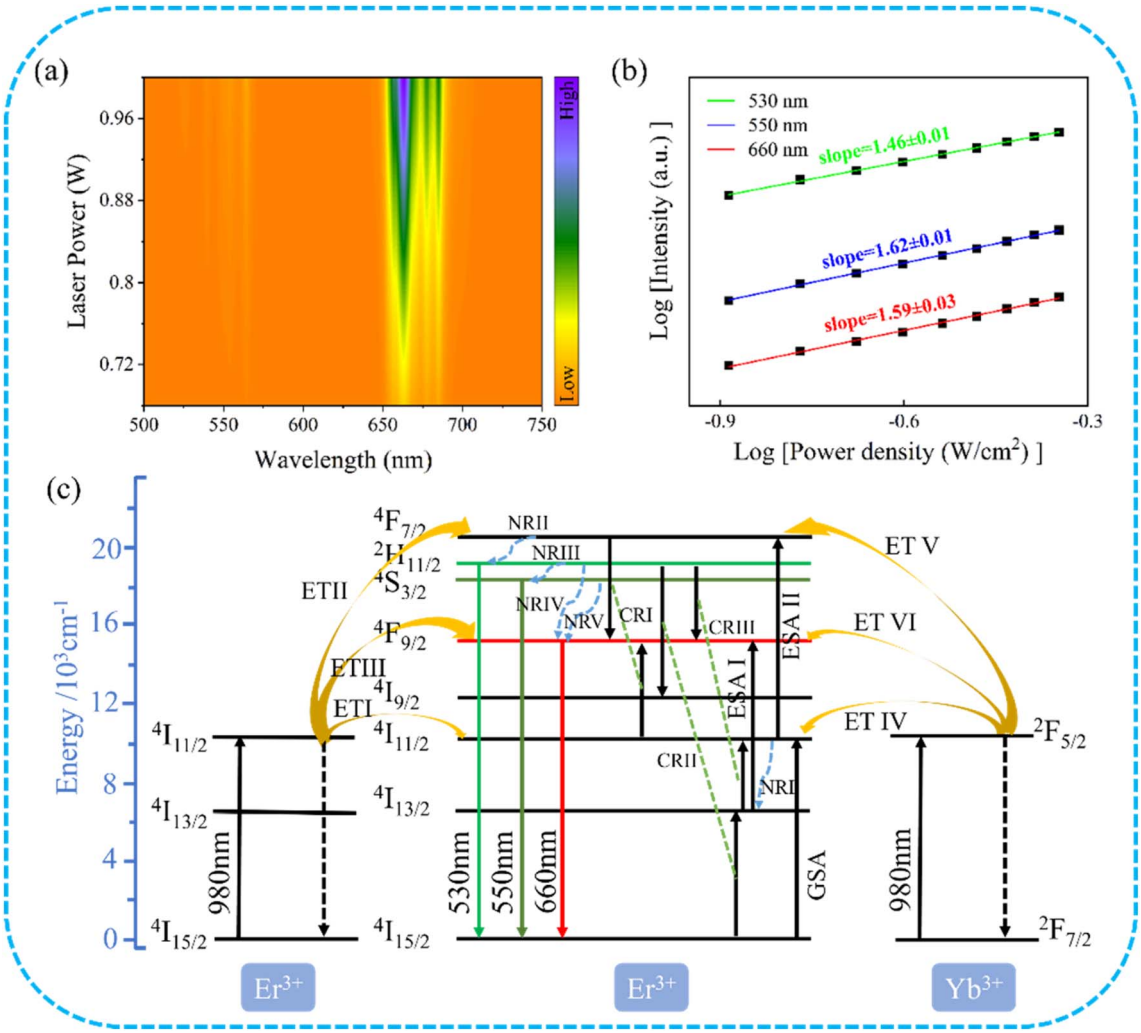

Fig. 4 (a) Pump power-dependent UCL spectra of $Ba_3Y(BO_3)_3$: 0.07 Er^{3+},0.21 Yb^{3+} under 980 nm laser excitation. (b) Logarithmic plots of pump power *versus* green and red emission intensities. (c) Energy level diagram and mechanism of $Ba_3Y(BO_3)_3$:0.07Er^{3+},0.21Yb^{3+}.

saturated excitation state, the luminescence intensity I is related to the excitation power P using the following equation:[47]

$$I = P^n, \tag{3}$$

where I is the luminescence intensity, P is the excitation power, and n is the number of photons required for up-conversion emissions. By taking the logarithms of both sides of the above equation, we obtain the following equation:

$$\log I = n \log P + C, \tag{4}$$

where C is a constant. Therefore the ratio (n) of $\log I/\log P$ indicates that the upconversion process can be attributed to n-photon absorption. A double logarithmic plot of the up-conversion luminescence intensity *versus* excitation power for $Ba_3Y(BO_3)_3$:0.07Er^{3+} and 0.21Yb^{3+} under different excitation powers of a 980 nm laser is shown in Fig. 4(b), where we can quantitatively analyze the relationship between light intensity and excitation power. The fitted curves for the three emission peaks are shown in the figure and closely match the experimental curves with minimal errors. The 530 nm green emission has a fitted slope of 1.46, the 550 nm green emission has a slope of 1.62, and the 660 nm red emission has a slope of 1.59. The values of n were close to 2, suggesting that the emission of the samples arose from a two-photon process.

To investigate the luminescence mechanism of $Ba_3Y(BO_3)_3$:0.07 Er^{3+},0.21Yb^{3+} phosphor, possible up-conversion emission processes are depicted in energy-level leap diagrams, as shown in Fig. 4c. Under excitation at 980 nm, Er^{3+} ions single doped or Er^{3+}–Yb^{3+} ions co-doped $Ba_3Y(BO_3)_3$ have a similar energy-transfer (ET) mechanism. Er^{3+} ions absorb a photon (980 nm) through a ground-state absorption (GSA) process, transitioning from $^4I_{15/2}$ to $^4I_{11/2}$, and Yb^{3+} ions absorb a photon (980 nm) through a GSA process, moving from $^2F_{7/2}$ to $^2F_{5/2}$. Compared to Er^{3+}, Yb^{3+} has a larger absorption cross-section, and its introduction improves energy transfer efficiency. For the Er^{3+}, Yb^{3+} co-doped $Ba_3Y(BO_3)_3$ phosphor, energy transfer (ET I) from Yb^{3+} to Er^{3+} can be expressed as follows: $^2F_{5/2}$ (Yb^{3+}) + $^4I_{15/2}$ (Er^{3+}) → $^2F_{7/2}$ (Yb^{3+}) +

© 2025 The Author(s). Published by the Royal Society of Chemistry

Open Access Article. Published on 09 June 2025. Downloaded on 4/8/2026 5:43:30 AM.
This article is licensed under a Creative Commons Attribution 3.0 Unported Licence.

$^4I_{11/2}$ (Er^{3+}). Some ions located at $^4I_{11/2}$ are transferred to the $^4I_{13/2}$ energy level by applying a non-radiative transition (NRI) process. Then, the ions at the $^4I_{13/2}$ energy level can absorb a photon to reach the $^4F_{9/2}$ energy level by excited-state absorption (ESA I). However, some Er^{3+} ions at the $^4I_{11/2}$ excited-state energy level is further excited to $^4F_{7/2}$ (ESA II) *via* energy transfer (ET II) from Yb^{3+} ions. The ions at the $^4F_{7/2}$ (Er^{3+}) energy level can gradually relax to the $^2H_{11/2}$, $^4S_{3/2}$ and $^4F_{9/2}$ energy levels by the radiation-less relaxation of NR II, NR III, NR IV, and NR V. The transitions between $^2H_{11/2} \rightarrow {}^4I_{15/2}$ energy levels correspond to green emission at 530 nm, the transitions between the $^4S_{3/2} \rightarrow {}^4I_{15/2}$ energy levels correspond to green emission at 550 nm, and the transitions between the $^4F_{9/2} \rightarrow {}^4I_{15/2}$ energy levels correspond to 660 nm. Furthermore, compared with the green emission, the red emission violently increases with the Yb^{3+} ion concentration, which is attributed to the decrease in the distance between the ions improving the efficiency of the cross-relaxation (CR): [$^4F_{7/2}$ (Er^{3+}) + $^4I_{11/2}$ (Er^{3+}) → $^4F_{9/2}$ (Er^{3+}) + $^4I_{9/2}$ (Er^{3+})] (CRI); [$^2H_{11/2}$ (Er^{3+}) + $^4I_{15/2}$ (Er^{3+}) → $^4I_{9/2}$ (Er^{3+}) + $^4I_{13/2}$ (Er^{3+})] (CRII); and [$^2H_{11/2}$ (Er^{3+}) + $^4I_{13/2}$ (Er^{3+}) → $^4F_{9/2}$ (Er^{3+}) + $^4I_{11/2}$ (Er^{3+})] (CRIII).

3.3 Optical temperature sensing performance of the samples

We investigated the temperature sensing performance of $Ba_3Y(BO_3)_3$:0.07Er^{3+},0.21Yb^{3+} phosphors. To reduce the heating effect of the laser, we used a low excitation power of 1.0 W. The variable-temperature emission spectra of the samples, measured between 90 K and 279 K, are shown in Fig. S4,† in which the PL intensity undergoes irregular changes with temperature. Under high temperature conditions, the variable-temperature emission spectra of the samples, measured between 333 and 513 K, are shown in Fig. 5(a). As the temperature increased, the intensity of the red emission decreased; however, the 530 nm emission intensity increased and the 550 nm emission initially increased before decreasing with temperature. Fig. 5(a) clearly shows the variations in green emission intensity. The increase in emission intensity with temperature may result from enhanced thermal mobility of ions from the lower to higher energy levels.

Er^{3+} ions have two thermally coupled energy levels, $^2H_{11/2}$ and $^4S_{3/2}$, with the number of ions at these levels following the Boltzmann distribution. Therefore, the intensities of the $^2H_{11/2} \rightarrow {}^4I_{15/2}$ (530 nm) and $^4S_{3/2} \rightarrow {}^4I_{15/2}$ (550 nm) emissions change with temperature. The fluorescence intensity ratio (FIR) of the two green emissions can be expressed as follows:[48]

$$\mathrm{FIR} = R = \frac{I_H}{I_S} = \frac{N\left(^2H_{11/2}\right)}{N\left(^2S_{3/2}\right)} = C\exp\left(\frac{-\Delta E}{kT}\right) \quad (5)$$

where I_H denotes the integral intensity of the $^2H_{11/2} \rightarrow {}^4I_{15/2}$ emission; I_S denotes to the integral intensity of the $^4S_{3/2} \rightarrow {}^4I_{15/2}$ emission; ΔE is the forbidden bandwidths of the two thermally coupled energy levels, $^2H_{11/2}$ and $^4S_{3/2}$; and K_B is the Boltzmann constant. Taking the logarithm of Ln for both sides of the above equation, we obtain the following equation:

$$\ln(\mathrm{FIR}) = \ln\frac{I_H}{I_S} = \left(\frac{-\Delta E}{kT}\right) + \ln C. \quad (6)$$

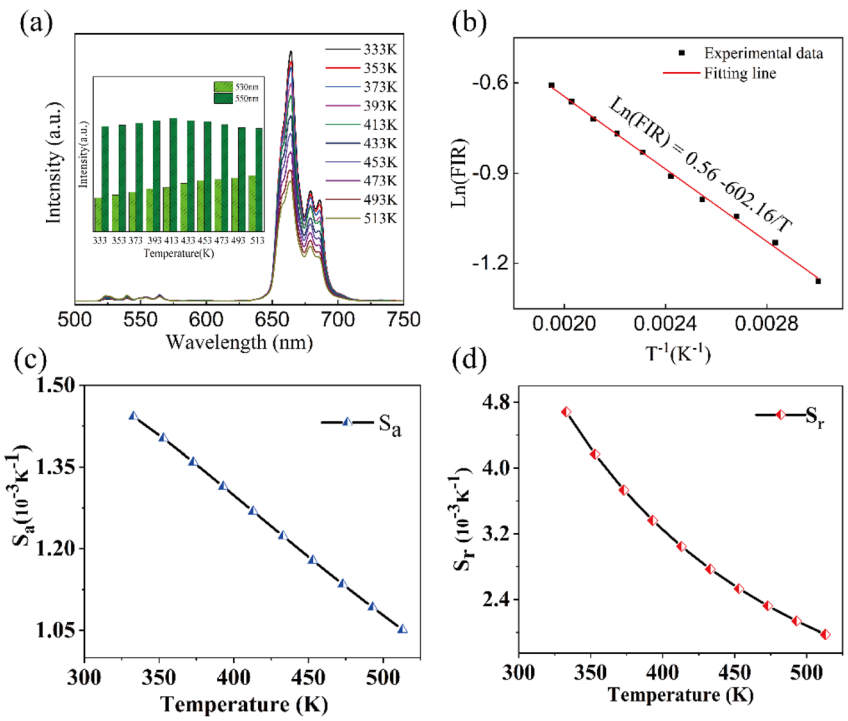

Fig. 5 (a) UCL spectra; (b) the integral intensity ratio of $^2H_{11/2} \rightarrow {}^4I_{15/2}$, $^4S_{3/2} \rightarrow {}^4I_{15/2}$, in Er^{3+} ions; (c) absolute sensitivity S_a; and (d) relative sensitivity S_r values of the $Ba_3Y(BO_3)_3$:0.07Er^{3+},0.21Yb^{3+} sample detected in the 303–573 K range under 980 nm laser excitation.

Open Access Article. Published on 09 June 2025. Downloaded on 4/8/2026 5:43:30 AM. This article is licensed under a Creative Commons Attribution 3.0 Unported Licence.

The absolute sensitivity (S_a) and relative sensitivity (S_r) are crucial parameters for evaluating temperature sensing and can be defined as eqn (7) and (8), respectively:[49]

$$S_a = \frac{dR}{dT} = R\frac{\Delta E}{kT^2} \quad (7)$$

$$S_r = \left|\frac{1}{R}\frac{dR}{dT}\right| = \frac{\Delta E}{kT^2} \quad (8)$$

The fitted curve of the linear relationship between Ln (FIR) and $1/T$ is shown in Fig. 5(b), where the linear relationship between ln(FIR) and $1/T$ is consistent with the linear relationship in eqn (4). The slope $\Delta E/k$ is 602.16, and the intercept ln C is 0.56. The calculated ΔE for the thermal coupling energy for this phosphor is consistent with previously reported values. The corresponding sensitivities S_a and S_r of $Ba_3Y(BO_3)_3$:0.07Er^{3+} and 0.21Yb^{3+} at different temperatures are shown in Fig. 5(c) and (d), respectively. It can be observed that the S_a and S_r of the phosphor reach their maximum values of 1.44×10^{-3} K^{-1} and 4.68×10^{-3} K^{-1} at 333 K, respectively. Table S2† shows some published results and compares them with the results of this study, which indicates that this material can be used as a candidate for temperature sensing.

4. Conclusion

In this study, novel up-conversion red phosphors of $Ba_3Y(BO_3)_3$ co-doped with Er^{3+} and Yb^{3+} were successfully synthesized using a high-temperature solid-phase method. Three emission bands at 530, 550, and 660 nm, corresponding to the $^2H_{11/2} \rightarrow {}^4I_{15/2}$, $^4S_{3/2} \rightarrow {}^4I_{15/2}$, and $^4F_{9/2} \rightarrow {}^4I_{15/2}$ of Er^{3+} ions, respectively, were observed under 980 nm excitation. The luminescence of $Ba_3Y(BO_3)_3$ maintains a high-purity red emission by modulating the doping concentration of Yb^{3+}. The introduction of Yb^{3+} ions enhanced the emission intensity of the samples. The luminescence mechanism was explained by the double logarithmic relationship between luminescence intensity and pump power. Additionally, the temperature sensitivity from 333 K to 513 K was explored using the FIR technique with two green emissions, achieving a maximum S_r of 1.44×10^{-3} K^{-1} at 333 K. These results demonstrate the potential applications of $Ba_3Y(BO_3)_3$:Er^{3+}/Yb^{3+} phosphors in luminescence and optical temperature sensing.

Data availability

The data supporting the findings of this study will be made available from the corresponding author upon request.

Author contributions

Lei Zhang and You Zhang: writing–original draft and investigation. Cuilin Jin: supervision, software, and investigation. Chunhao Wang: supervision, software, and investigation. Chunhao Wang and Qiongyu Bai: supervision, software, and investigation. Xu Li: writing–review & editing, supervision, and investigation. Yibo Zheng: writing–review & editing, supervision, software, and funding acquisition.

Conflicts of interest

The authors declare that they have no known competing financial interests or personal relationships that could have appeared to influence the work reported in this paper.

Acknowledgements

This work was partly funded by the S&T Program of Hebei, China (No. 22371701D), the Hebei Province Department of Natural Resources (No. 2024043) and the Hebei Province Optoelectronic Information Materials Laboratory Performance Subsidy Fund Project (No. 22567634H). We also appreciate the Excellent Going Abroad Experts' Training Program in Hebei Province.

References

1 J. Zhou, B. Del Rosal, D. Jaque, S. Uchiyama and D. Jin, Advances and challenges for fluorescence nanothermometry, *Nat. Methods*, 2020, **17**(10), 967–980.
2 A. Bednarkiewicz, J. Drabik, K. Trejgis, D. Jaque, E. Ximenes and L. Marciniak, Lanthanide-based nanothermometers for bioapplications: excitation and temperature sensing in optical transparency windows, *Appl. Phys. Rev.*, 2021, **8**(1), 011317.
3 C. D. S. Brites, R. Marin, M. Suta, A. N. C. Neto, E. Ximendes, D. Jaque and L. D. Carlo, Spotlight on luminescence thermometry: basics, challenges, and cutting-edge applications, *Adv. Mater.*, 2023, **35**(36), 2302749.
4 J. Chen, W. N. Zhang, S. F. Cui, X. S. Peng, F. F. Hu, R. F. Wei, H. Guo and D. X. Huang, Up-conversion luminescence properties and temperature sensing performances of Ba5Y8Zn4O21: Yb3+, Er3+ phosphors, *J. Alloys Compd.*, 2021, **875**, 159922.
5 X. W. Liu, B. C. Mei and G. L. Tan, Fabrication, microstructure and upconversion luminescence properties of Er:$Sr_5(PO_4)_3F$ transparent nanostructured ceramics, *J. Eur. Ceram. Soc.*, 2024, **44**(13), 7855–7866.
6 Y. Zhao, X. Wang, Y. Zhang, Y. Li and X. Yao, Optical temperature sensing of up-conversion luminescent materials: Fundamentals and progress, *J. Alloys Compd.*, 2020, **817**, 152691.
7 P. Du, L. Luo, H. K. Park and J. S. Yu, Citric-assisted sol-gel based Er^{3+}/Yb^{3+}-codoped $Na_{0.5}Gd_{0.5}MoO_4$: A novel highly-efficient infrared-to-visible upconversion material for optical temperature sensors and optical heaters, *Chem. Eng. J.*, 2016, **306**, 840–848.
8 X. Li, P. Gao, J. Li, L. Guan, X. Li, F. Wang, D. Wang, Z. Li and X. Li, Enhancing upconversion emission and temperature sensing modulation of the $La_2(MoO_4)_3$: Er^{3+}, Yb^{3+} phosphor by adding alkali metal ions, *Ceram. Int.*, 2020, **46**(13), 20664–20671.

© 2025 The Author(s). Published by the Royal Society of Chemistry

Open Access Article. Published on 09 June 2025. Downloaded on 4/8/2026 5:43:30 AM. This article is licensed under a Creative Commons Attribution 3.0 Unported Licence.

9 Q. Wang, H. Wu, L. Zhang, H. Wu, Y. Luo, G. Pan, Z. Hao, Q. Mu and J. Zhang, Green upconversion luminescence of Er^{3+} and Yb^{3+} codoped $Gd_2Mo_4O_{15}$ for optical temperature sensing, *J. Alloys Compd.*, 2022, **895**, 162516.

10 S. L. Ye and L. Lei, Controlled synthesis of cubic $NaYF_4$:Yb/Er@$NaYF_4$ core/shell nanocrystals for ratiometric fluorescence temperature sensing, *Chem. Phys. Lett.*, 2023, **833**, 140935.

11 L. Li, F. Qin, Y. Zhou, Y. Zheng, J. Miao and Z. Zhang, Three-energy-level-cascaded strategy for a more sensitive luminescence ratiometric thermometry, *Sens. Actuators, A*, 2020, **304**, 111864.

12 G. Xiang, Q. Xia, X. Liu and X. Wang, Optical thermometry based on the thermally coupled energy levels of Er^{3+} in upconversion materials, *Dalton Trans.*, 2020, **49**, 17115–17120.

13 H. Suo, X. Zhao, Z. Zhang, Y. Wang, J. Sun, M. Jin and C. Guo, Rational design of ratiometric luminescence thermometry based on thermally coupled levels for bioapplications, *Laser Photonics Rev.*, 2020, **15**(1), 2000319.

14 N. Zhang, M. S. Molokeev, Q. Liu and Z. Xia, Pure red upconversion luminescence and optical thermometry of Er^{3+} doped sensitizer-rich $SrYbInO_4$ phosphors, *J. Mater. Chem. C*, 2018, **6**(27), 7361–7366.

15 Q. Xiao, X. M. Yin, L. Lv, X. Y. Dong, N. Zhou, K. C. Liu and X. X. Luo, White up-conversion luminescence and highly-sensitive optical temperature sensing in $Na_3La(VO_4)_2$: Yb, Er, Tm, Ho phosphors, *J. Rare Earths*, 2023, **41**(7), 981–988.

16 X. Li, B. Bao, X. He, G. Wang, Y. Huang, L. Li and Y. Yu, Optical temperature sensing with an Er^{3+}, Yb^{3+} co-doped $LaBMoO_6$ single crystal, *J. Mater. Chem. C*, 2023, **11**, 2494–2504.

17 H. L. Gong, X. S. Peng, G. A. Ashraf, F. F. Hu, R. F. Wei and H. Guo, Dual-mode optical thermometry based on transparent NaY_2F_7: Er^{3+}, Yb^{3+} glass-ceramics, *Ceram. Int.*, 2022, **48**(3), 4023–4030.

18 F. Lu, L. Wang, F. Hu, X. Tian, H. Guo and R. Wei, Multipath luminescent thermometry in$Cs_3GdGe_3O_9$: Yb^{3+}, Er^{3+} phosphor, *Ceram. Int.*, 2022, **48**(24), 37186–37193.

19 Y. Tong, W. N. Zhang, R. F. Wei, L. P. Chen and H. Guo, $Na_2YMg_2(VO_4)_3$: Er^{3+}, Yb^{3+} phosphors: up-conversion and optical thermometry, *Ceram. Int.*, 2021, **47**(2), 2600–2606.

20 X. Yang, Y. Zhu, T. Li, S. Long and B. Wang, High-accuracy dual-mode optical thermometry based on up-conversion luminescence in Er^{3+}/Ho^{3+}-Yb^{3+} doped $LaNbO_4$ phosphors, *Ceram. Int.*, 2023, **49**(13), 21932–21940.

21 N. M. Bhiri, M. Dammak, M. Aguiló, F. Díaz, J. J. Carvajal and M. C. Pujol, Stokes and anti-Stokes operating conditions dependent luminescence thermometric performance of Er^{3+}-doped and Er^{3+}, Yb^{3+} co-doped $GdVO_4$ microparticles in the non-saturation regime, *J. Alloys Compd.*, 2020, **814**, 152197.

22 X. Li, X. Wang, H. Zhong, L. Cheng, S. Xu, J. Sun, J. Zhang, X. Li, L. Tong and B. Chen, Effects of Er^{3+} concentration on down-/up-conversion luminescence and temperature sensing properties in $NaGdTiO_4$: Er^{3+}/Yb^{3+} phosphors, *Ceram. Int.*, 2016, **42**(13), 14710–14715.

23 J. Liao, M. Wang, F. Lin, Z. Han, B. Fu, D. Tu, X. Chen, B. Qiu and H. R. Wen, Thermally boosted upconversion and downshifting luminescence in $Sc_2(MoO_4)_3$:Yb/Er with two-dimensional negative thermal expansion, *Nat. Commun.*, 2022, **13**(1), 1–11.

24 J. Hu, X. Bian, R. Wang, L. Liu, N. Ilyas, F. Wang, Z. Song and H. Fu, Giant Enhancement in Upconversion Luminescence of β-Ba_2ScAlO_5:Yb^{3+}/Er^{3+} Phosphor by the Intermediate Band through Ca^{2+} Doping, *Chem. Mater.*, 2022, **34**(7), 3089–3098.

25 X. L. Yan, Y. Z. Cao, X. K. Wang, J. S. Zhang, S. Xu, G. J. Li and B. J. Chen, Molten salt synthesized $LaTa_7O_{19}$:Er^{3+}/Yb^{3+} with superior upconversion luminescence using KCl flux, *J. Mater. Chem. C*, 2024, **12**, 13875–13883.

26 H. J. Zhang, X. B. Dong, L. Y. Jiang, Y. Yang, X. R. Cheng and H. M. Zhao, Comparative analysis of upconversion emission of LaF_3: Er/Yb and LaOF: Er/Yb for temperature sensing, *J. Mol. Struct.*, 2020, **1206**, 127665.

27 L. C. V. Rodrigues, H. F. Brito and A. Meijerink, Highly luminescent Gd_2O_2S: Er^{3+}, Yb^{3+} upconversion microcrystals obtained by a time-and energy-saving microwave-assisted solid-state synthesis, *J. Alloys Compd.*, 2023, **942**, 169083.

28 K. Maciejewska, A. Bednarkiewicz and L. Marciniak, NIR luminescence lifetime nanothermometry based on phonon assisted Yb^{3+}–Nd^{3+} energy transfer, *Nanoscale Adv.*, 2021, **3**, 4918–4925.

29 L. Yue, X. Zheng, P. Xia, C. Wang, Y. Lei, M. Xu and W. Dai, Structure and optical properties of stable Bi/Eu codoped borophosphate $La_7O_6(BO_3)(PO_4)_2$ phosphors for application in wLEDs, *Ceram. Int.*, 2024, **50**(7), 10947–10958.

30 K. Elzbieciak-Piecka and L. Marciniak, Optical heating and luminescence thermometry combined in a Cr^{3+}-doped $YAl_3(BO_3)_4$, *Sci. Rep.*, 2022, **12**, 16364.

31 P. Xia, W. Li, K. Wu, Y. Lei and W. Dai, Crystal Structure, Photoluminescence, and "Abnormal" High Stability of $Ca_3Y(GaO)_3(BO_3)_4$: Dy^{3+}/Sm^{3+}/La^{3+} for n-UV wLEDs, *Cryst. Growth Des.*, 2024, **24**(8), 3355–3369.

32 M. Oglakci, S. Akça-Özalp, Z. G. Portakal-Uçar, V. Correcher, J. F. Benavente, M. Sonsuz, N. Can, Y. Z. Halefoglu and M. Topaksu, Thermoluminescence study of Nd3+ doped lanthanum tri-borate phosphor, *J. Alloys Compd.*, 2025, **1013**, 178570.

33 X. Li, W. Dai, K. Nie, S. Li and M. Xu, Investigation on optical properties of borate $Sr_3Y_2B_4O_{12}$: Ce/Tb/Sm and its application in wLEDs, *J. Lumin.*, 2024, **53**, 14153–14162.

34 C. G. Ma, H. L. Chen, M. Luo, F. Y. Duan, Y. Ding, Y. H. Han, T. X. Zheng, X. Yang and Y. Xiao, A novel borate phosphor $Lu_5Ba_6B_9O_{27}$:Ce^{3+} codoped with Sr^{2+}/Tb^{3+} for NUV-white light emitting diode application, *Dalton Trans.*, 2023, **11**(6), 2202550.

35 S. Pan, Z. Hu, Z. Lin and G. Wang, Growth and X-ray diffraction of Nd^{3+}-doped $Ba_3Y(BO_3)_3$ crystal, *J. Cryst. Growth*, 2003, **247**, 452–456.

36 J. Zhao, X. Wang, Q. Pang and A. P. Zhang, Enhanced Near-Infrared Luminescence in Ba3Y(BO3)3: Nd3+ by Codoping with Ce3+, *ECS J. Solid State Sci. Technol.*, 2021, **10**, 016004.

© 2025 The Author(s). Published by the Royal Society of Chemistry

Open Access Article. Published on 09 June 2025. Downloaded on 4/8/2026 5:43:30 AM. This article is licensed under a Creative Commons Attribution 3.0 Unported Licence.

37 Q. Li, C. Chen, B. Shen, B. Yu and Y. P. Zhang, Enhanced red emission and high thermal stability from Bi^{3+}/Eu^{3+} co-doped $Ba_3Y(BO_3)_3$ phosphors for WLEDs application, *J. Lumin.*, 2021, **237**, 118196.

38 X. L. Wu, J. L. Zheng, Q. Ren, W. N. Bai, Y. H. Ren and O. Hai, Synthesis and luminescent properties of a novel orange-red $Ba_3Y(BO_3)_3:Sm^{3+}$ phosphors for white LEDs, *Polyhedron*, 2019, **164**, 17–22.

39 X. B. Qiao and H. J. Seo, Phase transition, structural and spectroscopic properties of $Ba_3Y(BO_3)_3$ phosphor, *J. Alloys Compd.*, 2015, **637**, 504–508.

40 W. W. Wu, Y. P. Zhang, Y. P. Zhang and J. X. Hu, $Ba_3YB_3O_9$ based phosphor ceramic plates withexcellent thermal stability for wLED applications, *Dalton Trans.*, 2021, **50**, 5287.

41 X. Z. Li, X. L. Chen, L. Wu, Y. G. Cao, T. Zhou and Y. P. Xu, $Ba_3YB_3O_9$: phase transition and crystal structure, *J. Alloys Compd.*, 2004, **370**, 53–58.

42 W. Liu, S. Q. Xu and L. Lei, Enhancing upconversion of $Sc_2Mo_3O_{12}$:Yb/Ln (Ln = Er, Ho) phosphors by doping Ca^{2+} ions, *Opt. Mater.*, 2023, **143**, 114166.

43 K. Saidi, C. Hernández-Álvarez, M. Runowski, M. Dammak and I. R. M. Benenzuela, Temperature and Pressure Sensing Using an Optical Platform Based on Upconversion Luminescence in $NaSrY(MoO_4)_3$ Codoped with Er^{3+} and Yb^{3+} Nanophosphors, *ACS Appl. Nano Mater.*, 2023, **6**, 19431–19442.

44 J. P. Ma, Y. M. Chen, L. M. Zhang, S. Q. Guo, J. D. Liu, H. Li, B. J. Ye, Z. Y. Li, Y. Zhou, B. B. Zhang, O. M. Zhang and H. T. Sun, Insights into the local structure of dopants, doping efficiency, and luminescence properties of lanthanide-doped $CsPbCl_3$ perovskite nanocrystals, *J. Mater. Chem. C*, 2019, **7**(10), 3037–3048.

45 K. M. Zhu, Z. Y. Wang, H. Y. Xu and Z. L. Fu, Development of Multifunctional Materials Based on Heavy Concentration Er^{3+}-Activated Lead-free Double Perovskite $Cs_2NaBiCl_6$, *Adv. Opt. Mater.*, 2022, **10**, 2201182.

46 H. Jin, N. Fu, C. H. Wang, C. X. Qi, Z. Y. Liu, D. W. Wang, L. Guan, F. H. Wang and X. Li, Sr/Ba substitution induced higher thermal stability far red-emitting $Ba_{1-y}Sr_yLaLiWO_6:Mn^{4+}$ phosphors for plant growth applications, *Dalton Trans.*, 2023, **52**, 787–795.

47 S. M. Wei, Y. Q. Yang and Z. H. Li, The Mn/Yb/Er triple-doped CeO_2 nanozyme with enhanced oxidase-like activity for highly sensitive ratiometric detection of nitrite, *Chin. Chem. Lett.*, 2024, **35**(6), 109114.

48 J. X. Jiao, Y. W. Liu, H. Wang, X. M. Yin, M. M. Xing, X. X. Luo and Y. Tian, Enhancing upconversion luminescence and thermal sensing properties of Er/Yb co-doped oxysulfide core-shell nanocrystals, *J. Am. Ceram. Soc.*, 2021, **104**(2), 985–994.

49 K. He, L. Zhang, Y. Liu, B. Xu, L. Chen and G. Bai, Lanthanide ions doped nonhygroscopic $La_2Mo_3O_{12}$ microcrystals based on multimode luminescence for optical thermometry, *J. Alloys Compd.*, 2022, **890**, 161918.

© 2025 The Author(s). Published by the Royal Society of Chemistry